Macromolecular Materials and Engineering
Open Access
www.mame-journal.de

Femtosecond Laser Transmission Joining of Fused Silica and Polymethyl Methacrylate

Felice Alberto Sfregola, Raffaele De Palo, Caterina Gaudiuso, Pietro Patimisco, Antonio Ancona, and Annalisa Volpe*

In this study, polymethyl methacrylate (PMMA) is joined with fused silica using pulsed femtosecond laser transmission micro-welding. This technique enables the welding of transparent materials to each other without the need for intermediate opaque layers, through localized energy deposition. The laser parameters – peak fluence, scanning speed, and hatch distance – are systematically optimized to maximize joint shear strength. The ATR-FTIR spectroscopic analysis has proven that mechanical interlocking is the primary mechanism of joint formation between the two materials. An analytical model based on heat accumulation is developed to describe the joining process, with a good predictive quality confirmed by comparison with the experimental results. This joining approach is applied to seal a hybrid PMMA-fused silica microfluidic chip. The device has successfully passed a static leakage test by withstanding pressures up to the full-scale value of the employed microfluidic pump at 2 bar, demonstrating the effectiveness of femtosecond laser transmission welding for fabricating robust and reliable joints in hybrid microfluidic devices.

1. Introduction

In recent years, polymers have become the materials of choice for disposable Lab-on-a-Chip devices due to their versatility, ease of fabrication, and advantageous physical and chemical properties. Among various thermoplastics, polymethyl methacrylate (PMMA) stands out due to its unique physical and chemical properties that make it particularly suitable for microfluidic applications. PMMA is biocompatible, optically transparent, and demonstrates excellent mechanical strength and chemical resistance.[1] Moreover, its adaptability is further highlighted by the broad range of compatible fabrication techniques, including laser micromachining, photolithography, injection molding, and hot embossing.[2]

Despite these advantages, the integration of PMMA with non-polymer substrates such as glass, piezoelectric materials, semiconductors, and ceramics presents significant challenges. This is particularly relevant as the need for hybrid structures and components increases across various industries, including automotive, microelectronics, aerospace, and healthcare.[3,4]

Various bonding techniques between thermoplastic components, including lamination, ultrasonic welding, and thermo-compression bonding, have been successfully employed to seal microchannels within PMMA devices.[2,5] However, achieving robust and reliable bonding of polymers to non-polymer substrates remains problematic due to their differences in physical and chemical properties. Conventional strategies, including adhesive-based methods, lamination bonding, localized heating[5], and surface activated bonding,[6] have been explored to overcome these bonding challenges. However, these methods often require complex, expensive, and time-consuming processes, as well as the use of glues or intermediate films, which can lead to issues such as solvent outgassing, biocompatibility concerns, and environmental threats.

In this context, laser transmission welding (LTW) has emerged as a promising technique for joining thermoplastic polymers[7] and polymer-metal hybrid structures.[8] This non-contact direct bonding technique involves transmitting a laser beam through a transparent polymer and focusing it at the interface with an opaque substrate. The absorbed laser energy is converted into heat, leading to localized melting and subsequent bonding upon cooling. Compared with other joining methods, laser welding is fast, precise, reliable, and compatible with automation.[8] Traditional LTW faces significant limitations when joining transparent materials due to the need for light-absorbing intermediate layers. This is where ultrafast laser technology becomes advantageous.

Ultrafast lasers, with their extremely short pulse durations and high peak intensities, induce nonlinear absorption processes in transparent materials, enabling energy deposition in the focal

F. A. Sfregola, R. De Palo, P. Patimisco, A. Ancona, A. Volpe
Intercollegiate Department of Physics "M. Merlin"
University of Bari and Polytechnic University of Bari
Via G. Amendola 173, Bari 70125, Italy
E-mail: felice.sfregola@uniba.it
F. A. Sfregola, R. De Palo, C. Gaudiuso, A. Ancona, A. Volpe
Institute for Photonics and Nanotechnologies (IFN)
National Research Council (CNR)
Via G. Amendola 173, Bari 70125, Italy
The ORCID identification number(s) for the author(s) of this article can be found under https://doi.org/10.1002/mame.202400354

DOI: 10.1002/mame.202400354

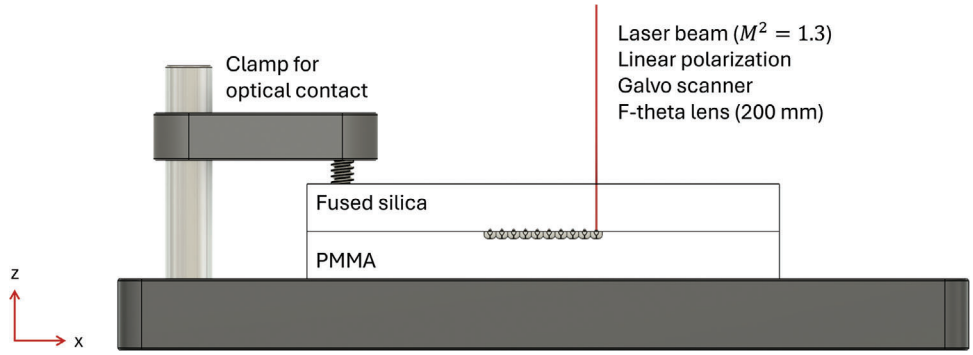

Figure 1. Schematic of the clamping setup. The sample holder is provided with an XYZ linear translation stage.

volume that can be precisely located at the interface between the substrates in order to induce confined materials modification without the need for additional absorbing layers.[9] Bond formation in ultrafast LTW depends on the physical, chemical, and optical properties of the involved materials, as well as the laser parameters, such as pulse duration, peak fluence, repetition frequency, and focal position.[10] The complex interplay of these factors prevents a straightforward and comprehensive understanding of the process. Consequently, a systematic optimization of the laser parameters is required on a case-by-case basis, often achieved through empirical or statistical approaches.[10]

Ultrafast LTW has been widely employed for bonding of transparent hard and brittle (THB) materials and THB material-metal hybrids,[11] but recently has also been applied to polymers. Femtosecond lasers have been employed to weld homogeneous transparent polymers, such as PMMA[12] and cyclo-olefin copolymers,[13] and to bond hybrid polymer-semiconductor structures like PMMA-silicon.[14] However, the use of ultrafast LTW for joining transparent polymers to THB materials is yet to be explored.

In this work, the feasibility of joining PMMA to fused silica by femtosecond laser transmission microwelding was investigated. The influence of peak fluence, scanning velocity, and weld pattern on the bonding strength was studied through a push-test configuration. Morphological and spectroscopic analyses of joint interfaces provided insights into the nature of the bond. The bond formation was further studied by developing an analytical heat accumulation model. Finally, a microfluidic PMMA-fused silica hybrid device was sealed using the developed femtosecond LTW technique and its performance was evaluated through a static leakage test.

2. Results and Discussion

2.1. Influence of Laser Working Parameters

In this study, high-purity optical-quality fused silica and polymethyl methacrylate (PMMA) substrates were stacked on top of each other and clamped together, as schematized in **Figure 1**. The linearly polarized Gaussian laser beam, emitting at 1030-nm wavelength, was focused on the interface between the two substrates with a 100- mm focal length *f*-theta lens coupled to a Galvo scanner. This arrangement ensured that both materials were within the effective focal depth of the laser, keeping the laser-induced plasma and melted material confined at the interface.[15] This condition, known as optical contact, is verified when the gap between two substrates is below a quarter of the wavelength and interference fringes, specifically, Newton's ring pattern, are observed.

Table 1. Operating laser parameters analyzed during the process optimization.

Parameter	Value
Scanning velocity v_s [mm s^{-1}]	1 – 10 – 100
Peak fluence F_0 [J cm^{-2}]	0.79 – 1.06 – 1.32 – 1.59 – 1.85 – 2.11
Hatch spacing h [µm]	50 – 100 – 200 – 300 – 400 – 500 – 600 – 800

The clamping setup was fixed on a 3-axis manual linear translation stage (resolution of 10 µm) to facilitate the positioning of the interface at the focal plane of the *f*-theta lens. The optimal focusing position, which enabled continuous laser-induced modification on both sides of the interface, was found by performing a z-scan procedure which consisted in writing several laser traces at different z-heights over a range of 400 µm centered at the interface with steps of 50 µm.[16] This optimization is crucial for achieving reliable and strong bonding between transparent materials due to the high localization of the focused beam and, therefore, of the laser-induced material modifications.[9]

The strength of a joint achieved through ultrafast laser welding is significantly influenced by the laser working parameters, specifically the repetition frequency, scanning velocity, and peak fluence.[10] These parameters control the laser energy deposited per unit area and time, thereby determining the laser-matter interaction and weld formation. At a fixed repetition frequency f_r of 200 kHz, the impact of the other two parameters was analyzed by scanning single 3-mm lines for each set of values listed in **Table 1**.

The range of investigated pulse peak fluence was selected to match the ablation threshold fluences of the two materials,[17,18] while the scanning velocities were chosen to ensure a sufficient number of pulses per spot ($N_p > 50$) for heat accumulation phenomena to occur.[17,18]

Figure 2 shows the optical microscope images acquired at the interface between the two substrates after the laser welding process with representative sets of working laser parameters. It was found that for velocities greater than 1 mm s^{-1} and peak fluences below 1 J cm^{-2}, a strong and durable bond could not be

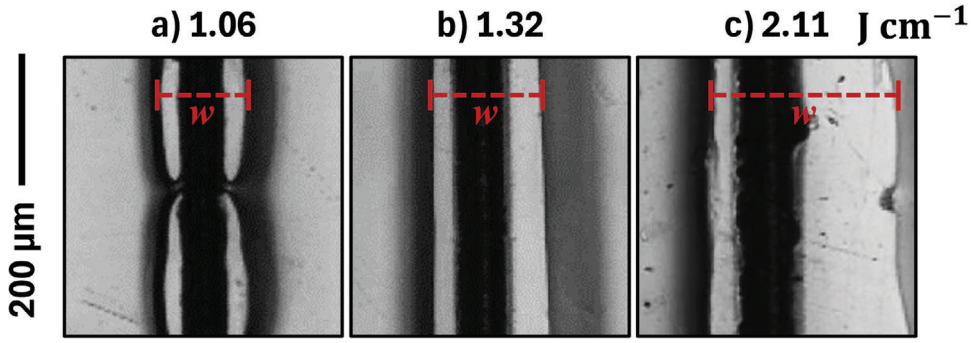

Figure 2. Optical microscope images in transmission mode of the welded single lines on the interface at $\nu_s = 1$ mm s^{-1} and representative peak fluences of a) 1.06, b) 1.32, and c) 2.11 J cm^{-1}. The red dashed lines highlight the width of the melted track.

achieved. Microscope images reveal that the weld seam is characterized by an ablation line surrounded by a modified area, whose width w is significantly influenced by the peak fluence. This suggests that the PMMA substrate underwent thermal modification rather than pure ablation during the welding process, as it will be further shown in the subsequent sections. A repeatable and homogeneous weld was achieved at $F_0 = 1.32$ J cm^{-2} (Figure 2b), with an average melted track width of 129 ± 3 µm. Conversely, at peak fluences above 2 J cm^{-2} (Figure 2c), a bond was consistently formed but the weld seam was inhomogeneous and varied in extent with each test, even under identical irradiation conditions.

The chosen weld pattern consisted of an array of parallel scanning lines with a fixed distance determined by the hatch spacing h. The weld strength at different h values (see Table 1) was evaluated using a custom shear break testing rig (see Section 4).[14] **Figure 3a** shows the dependence of the measured shear strength S on the hatch spacing h at fixed laser parameters (F_0 = 1.32 J cm^{-2}, ν_s = 1 mm s^{-1}). The observed behavior, which peaks at h = 200 µm, can be explained considering the trade-off between the width w of the melted track and the hatching distance.[14]

As shown in Figure 3b, when $h/w > 1$, the scanning lines are well separated, resulting in a reduced effective welding area that does not uniformly cover the processed area, thus leading to low bonding strength. Conversely, if $h/w < 1$, the laser-melted tracks of adjacent scanning lines overlap, meaning that scanning lines are produced on already modified zones rather than pristine material. As observed by Richter et al.,[19] the melting and subsequent quenching during the welding process induce tensions and stresses in the material which act as predetermined breaking points, reducing the ultimate joint strength. Consistently with these considerations, the maximum shear strength was achieved at a hatch spacing close to the average weld seam width ($h/w \approx 1$), which provided a uniformly covered welding area is with minimal overlap. A similar trade-off behavior has been reported for fs-laser bonding of silicon to PMMA,[14] and welding of similar and dissimilar glasses.[9]

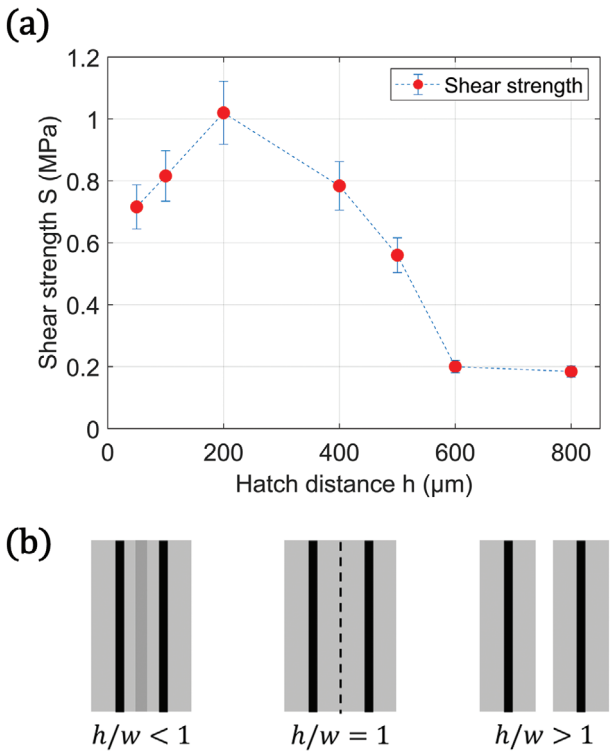

Figure 3. a) Shear strength of bonded samples as a function of the hatch distance h at F_0 = 1.32 J cm^{-2} and ν_s = 1 mm s^{-1}. The higher shear strength is obtained at h = 200 µm. Data points are connected by straight dashed lines only for enhanced visualization. b) Sketches of the overlap between consecutive scanning lines for different ratios of h/w.

2.2. The Joining Mechanism

To understand the bonding mechanism at the interface between PMMA and fused silica, a detailed analysis of the weld seam morphology was conducted through SEM imaging (**Figure 4**). The SEM images of the two materials after breaking the bond revealed distinct features in both the non-joined and joined areas. The non-joined fused silica (Figure 4a) exhibited an ablation track less than 10-µm wide, characterized by a series of grooves that increased the surface roughness. In the joint region of the fused silica (Figure 4b), the processed area presented what seemed to be a layer deposited on the substrate covering up the grooved surface. This experimental evidence suggested that PMMA melted, spread across the interface, and then resolidified during the welding process, remaining attached to the fused silica substrate after

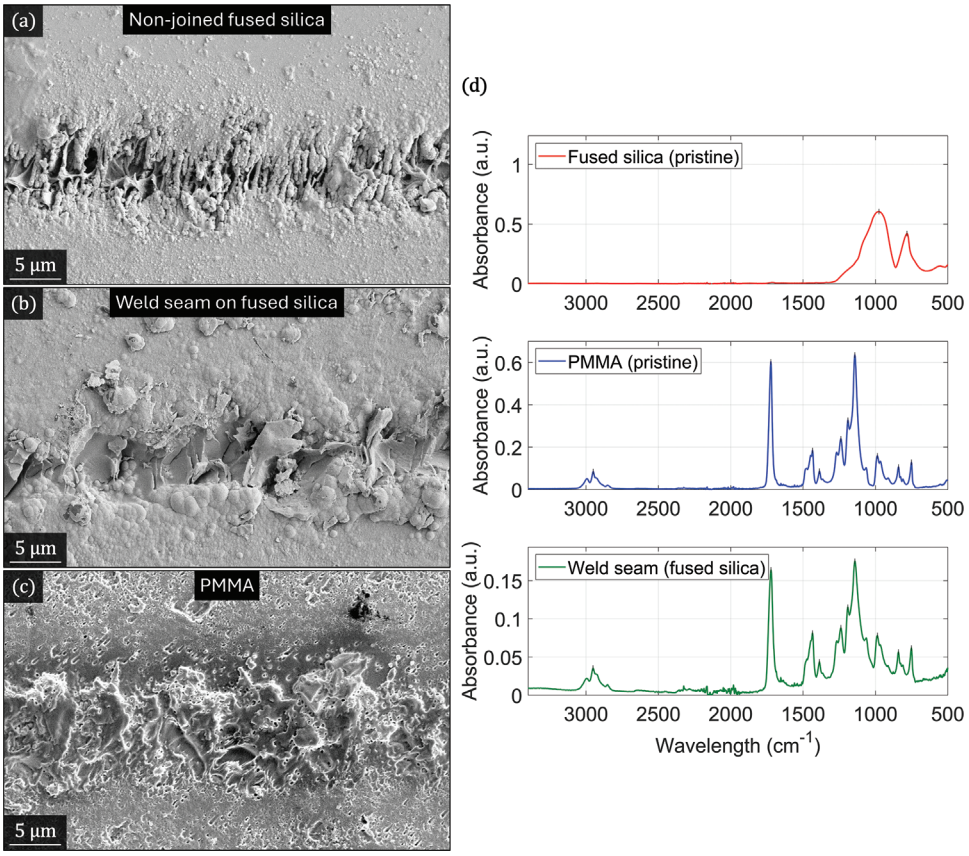

Figure 4. SEM images of the a) non-joined area of the fused silica, b) weld seam on the joined area of the fused silica, and c) PMMA. d) ATR-FTIR spectra of the two pristine materials and the weld seam.

the bond was broken. Finally, the SEM image of the PMMA (Figure 4c) displayed a melted track of comparable width to the weld seam observed in fused silica. These findings suggest the formation of a mechanical bond through an anchorage mechanism, where the rough, grooved surface of the fused silica interlocked with the melted and solidified PMMA, enhancing the joint's strength and stability. This bonding mechanism has already been observed for the laser joining of PMMA hybrid structures with silicon,[14] alumina ceramic[20], and stainless steel.[21]

The chemical properties of the bond were investigated through ATR-FTIR spectroscopy, first by analyzing the two pristine materials individually and then by examining the joined area on the fused silica substrate after breaking the bond. As shown in Figure 4d, the spectrum of the weld seam exhibited peaks identical to those of the pristine PMMA spectrum, indicating the presence of a layer of PMMA still attached to the fused silica substrate. Specifically, the spectrum included bands corresponding to the alkyl groups (CH_3 and CH_2) stretching at 2950 cm^{-1} and the PMMA characteristic band at 1720 cm^{-1} ascribed to the carbonyl group (C═O) stretching.[22] Although the weld seam spectrum did not exhibit significant macromolecular changes compared to pristine PMMA, slight modifications were observed. These included variations in the absorbance of PMMA characteristic bands, which could be attributed to oxidative photodegradation of the polymer during the welding process.[22] This degradation can be quantified by the carbonyl index, calculated as the ratio of maximum absorptions of carbonyl group stretching to alkyl group stretching.[23] The carbonyl index decreased from 7.10 in the pristine material to 4.66 in the weld, indicating chain scission via photooxidative processes due to the intense laser-matter interaction.[24] This degradation has probably compromised the polymer's mechanical behavior, reducing its tensile strength,[22] which may contribute to a reduction in the maximum shear strength of the bond, as previously discussed. Finally, the baseline below 2000 cm^{-1} for the weld seam spectrum can be attributed to a minor and broad contribution from the fused silica substrate, upon which the melted PMMA is deposited.

2.3. The Role of Incubation on Heat Accumulation

The proposed interlocking mechanism responsible for the bonding at the interface between PMMA and fused silica relies on the different responses of the two materials to laser irradiation. Experimental evidence suggests that PMMA, with a glass transition temperature of 110 °C, melts when exposed to laser radiation, while fused silica, with a significantly higher glass transition temperature of 1200 °C,[25] undergoes pure ablation. The temperature distribution in the two materials after irradiation with a series of fs-pulses can be calculated using the heat accumulation model developed by Weber et al.[26] This model, based on the solutions of the heat conduction equation introduced by

N.N. Rykalin, has been already used to describe the laser welding process in dissimilar materials.[14] According to this model, the temperature increase caused by heat accumulation after a series of N_p laser pulses delivered with a repetition frequency f_r is given by:

$$T\left(N_p, r\right) = T_0 + \frac{2 \cdot Q_H}{\rho c_p \sqrt{\left(\frac{4\pi\kappa}{f_r}\right)^{nD}}} \sum_{N=1}^{N_p} \frac{1}{\sqrt{N^3}} \exp\left[-\left(\frac{r^2}{4\kappa}\right) / \left(\frac{N}{f_r}\right)\right] \tag{1}$$

where $r^2 = x^2 + y^2 + z^2$ and x, y, z are the spatial coordinates. Here, T_0 is the initial temperature, ρ is the mass density of the material, c_p its specific heat capacity, $\kappa = \lambda_{\text{th}}/(\rho \bullet c_p)$ is the temperature conductivity, λ_{th} is the heat conductivity. The material properties are assumed to be constant and temperature-independent. Furthermore, the pulses are considered to have a Gaussian spatial distribution and negligible duration compared to the thermal diffusion timescale. The factor of 2 is introduced when the heat source is on a surface, allowing heat to flow only into one-half space. The thermal energy Q_H is defined as the fraction of total absorbed incident laser pulse energy E_p converted into heat:

$$Q_H = \eta_H \cdot E_P \tag{2}$$

where η_H is a time-dependent function of both the material properties and the laser processing parameters, particularly the incident fluence and the ablation threshold fluence $F_{\text{th}}(N)$, defined as the minimum laser fluence to start the ablation process.[27] In Weber et al.[26] this fraction is assumed to be constant and left as a free-fitting parameter. However, as reported by Ben-Yakar et al.,[28] η_H can be defined as the ratio of the energy required to raise the temperature of a material unit volume to the melting point over the energy required to ablate the same volume, and it can be expressed as

$$\eta_H = \frac{\rho c_p \left(T_m - T_0\right)}{E_p / V} \tag{3}$$

where T_m is the melting temperature, T_0 is the initial temperature of the material and V is the single-pulse ablation volume. For amorphous materials such as fused silica and PMMA, which do not have a defined melting point but instead transition from a brittle, glassy state to a more ductile, rubbery state with increasing temperature,[29] the glass transition temperature T_g was used in place of the melting temperature. In the case of femtosecond laser ablation of borosilicate glass, only a tiny fraction of the input energy (≈0.47 %) is used to melt the ablation volume.[28] This result is not surprising because ultra-fast laser-material interactions are primarily driven by non-thermal processes,[30], and most of the absorbed energy is actually used to vaporize and remove the ablated material from the surface.[31]

The ablation volume V could be estimated by evaluating the volume integral over the Gaussian profile of the crater:[28]

$$V = 2\pi \int_0^{D/2} r h_a(r)\, dr \tag{4}$$

where r is the radial distance from the center of the crater. D and h_a are the diameter and the depth of the ablated crater, respectively, and can be measured. The estimated volume is ≈ 50%–60% of the volume of the cylinder enclosing the crater profile.[28] The ablation volume scales linearly with the squared logarithm of the laser fluence because D^2 and h_a depend separately on the logarithm of the fluence.[28]

According to Liu et al.,[32] the squared diameter D^2 of craters ablated by pulsed Gaussian laser beams is related to the ablation threshold fluence $F_{\text{th}}(N)$ through the following equation:

$$D^2 = 2w^2 \ln\left(\frac{F_0}{F_{th}(N)}\right) \tag{5}$$

where F_0 is the peak laser fluence defined as:

$$F_0 = \frac{2E_p}{\pi w^2} \tag{6}$$

and w is the $1/e^2$ Gaussian beam radius, i.e., the spot size. A similar relationship can also be found for the ablation depth per pulse h_a:[28]

$$h_a = \alpha_{eff}^{-1} \ln\left(\frac{F_0}{F_{th}(N)}\right) \tag{7}$$

where ${\alpha_{\text{eff}}}^{-1}$ can be interpreted as the "effective optical penetration depth" of the laser radiation as expected from the Beer-Lambert law. This ablation regime is only accessible with subpicosecond laser pulses. For pulse lengths longer than 1 ps, the ablation threshold shifts to higher values, and the macroscopic ablation threshold is defined by the effective heat penetration depth rather than the optical penetration depth.[33]

The ablation threshold $F_{\text{th}}(N)$ depends both on the material's properties and the laser parameters.[34] Furthermore, it has been experimentally observed for several materials, including THB dielectrics[35,36] and polymers,[17] that by irradiating their surfaces with a series of N consecutive pulses, their ablation threshold lowered.[37] This phenomenon, known as the "incubation effect", is often described through different mathematical models that relate the multi-pulse ablation threshold $F_{\text{th}}(N)$ to the single-pulse threshold $F_{\text{th},1}$. For both fused silica[18] and PMMA[17] the accumulation mechanism is better described by a power law:

$$F_{th}(N) = F_{th,1}\, N^{S-1} \tag{8}$$

where $0 < S < 1$ is an empirical parameter that quantifies the strength of the incubation in the target material and is known as the incubation coefficient. This relationship, along with Equation 5 and Equation 6, enables the evaluation of the single-pulse ablation volume V for the N-th pulse based on the materials parameters available in the literature, eliminating the need for direct measurements. Consequently, Equation 1 can be rewritten without free-fitting parameters as:

$$T\left(N_p, r\right) = T_0 + \frac{2 \cdot \left(T_g - T_0\right)}{\sqrt{\left(\frac{4\pi\kappa}{f_r}\right)^{nD}}} \sum_{N=1}^{N_p} \frac{V(N)}{\sqrt{N^3}} \exp\left[-\left(\frac{r^2}{4\kappa}\right) / \left(\frac{N}{f_r}\right)\right] \tag{9}$$

Table 2. Parameters values used for PMMA and fused silica in the heat accumulation model.

Parameter	PMMA	Fused silica
Mass density ρ [g cm^{-3}]	1.18	2.20
Specific heat capacity c_p [J kg^{-1} K^{-1}]	1466	740
Heat conductivity λ_{th} [W m^{-1} K^{-1}]	0.25	1.38
Effective absorption coefficient α [cm^{-1}]	$1.45 \cdot 10^4$ [17]	$7.3 \cdot 10^4$ [18]
Ablation threshold fluence $F_{th,1}$ [J cm^{-2}]	2.6[17]	2.1[18]
Incubation coefficient S	0.67[17]	0.76[18]

This formulation for the heat accumulation model highlights the role of incubation on the temperature distribution during pulsed materials processing. Moreover, it provides a straightforward approach for estimating the laser parameters, such as peak fluence F_0 and repetition frequency f_r, required to either achieve material fusion or prevent it, depending on the specific properties of the materials involved. The parameters used in this study for PMMA and fused silica are listed in **Table 2**.

The model was employed to simulate the temperature distribution within both materials for each set of working laser parameters listed in Table 2. To simplify the analysis, an equal energy distribution between the two materials at the interface was assumed, and a single irradiated spot was considered instead of scanning lines. The number of incident pulses N_P was calculated based on the spot size ($w = 16$ µm) using the formula $(2w \cdot f_r)/v_s$.[14] The effective pulse overlap PO(%) of consecutive laser pulses was also taken into account by using the formula $(1 - v_s/(2w \cdot f_r)) \cdot 100$.[36]

For the fused silica, the model predicts a maximum temperature of ≈106 °C at the highest peak fluence and pulse number ($F_0 = 2.11$ J cm^{-2}, $N_P = 6400$, PO = 99.98 %). This temperature value is insufficient to cause thermal modification of the material,[25] supporting the experimental evidence that fused silica undergoes non-thermal ablation.

Conversely, the laser parameters play a crucial role in influencing the melting behavior of the PMMA substrate due to its relatively low glass transition temperature. The width of the melted track was determined by evaluating the area of the temperature distribution exceeding 70 °C, at which the material begins its transition from the glassy to the viscoelastic phase.[38] **Figure 5a** presents the temperature distribution simulated by using Equation 9 for the laser parameters ($F_0 = 1.32$ J cm^{-2}, $v_s = 1$ mm s^{-1}) set during the welding process, showing a predicted melted track width of 128.73 µm, compatible with the measured value of 129 ± 3 µm.

Experimental measurements of the melted track width, evaluated as the average along single scanning lines, were compared with simulation results for each set of laser parameters. Figure 5b shows these results plotted as a function of the peak fluence for $v_s = 1$ mm s^{-1}, demonstrating the model's accuracy with an adjusted $R^2 = 0.89$. Similar results were observed for $v_s = 10$ mm s^{-1}, confirming that for melted track widths less than 70 µm, strong and repeatable bonding could not be achieved. These findings validate the proposed model as a reliable tool for designing laser processing experiments.

2.4. Proof of Concept: Microfluidic Channel Sealing and Testing

The optimal operating parameters for achieving maximum joint shear strength were employed to assemble a hybrid microfluidic chip, following the procedure developed by Capodacqua et al.[14] (see Section 4), as depicted in **Figure 6a**. The weld seam, consisting of five scanning lines that follow the profile of the channel and the two reservoirs, covers an effective width of ≈1 mm and does not hinder the optical clarity of the device. As shown in Figure 6b, the ablation lines and the melt spread are confined to the immediate vicinity of the scanning lines, thus preventing any potential clogging of the microfluidic channel. These observations demonstrate the technique's applicability to real-world scenarios.

The performance of the assembled microfluidic system was determined through a static sealing test developed by Rasponi et al.[39] (see Section 4). The chip passed the test, withstanding pressures up to 2 bar, which corresponds to the full-scale value of the employed microfluidic pump. In comparison, similar tests on hybrid silicon-PMMA[14] and homogeneous PMMA[12] devices, assembled using the same procedure, exhibited maximum pressure tolerances of 30 mbar and 1 bar, respectively. Conversely, a similar hybrid PDMS–Glass bond,[40] achieved through plasma bonding, exhibited a maximum bonding strength of 0.51 MPa

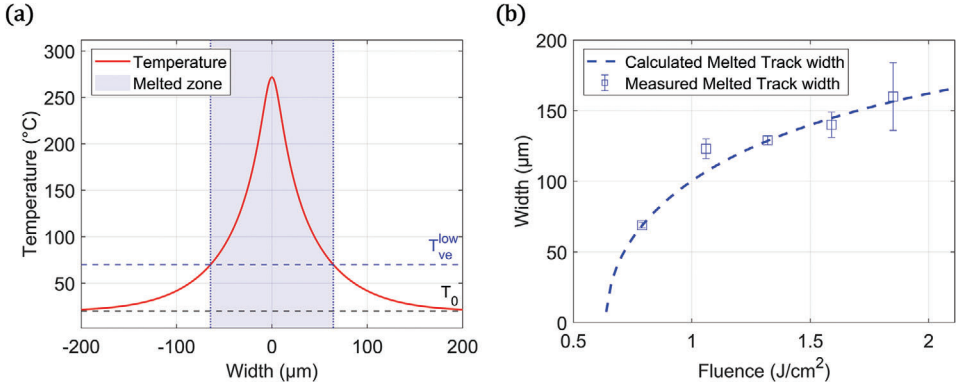

Figure 5. a) Temperature radial distribution in PMMA calculated for $F_0 = 1.32$ J cm^{-2} and $v_s = 1$ mm s^{-1}. In the blue area the temperature is above 70 °C, resulting in the material being in a melted state. b) Laser-melted track widths as a function of the peak fluence F_0. The experimental data are fitted with the simulated results from the developed heat accumulation model.

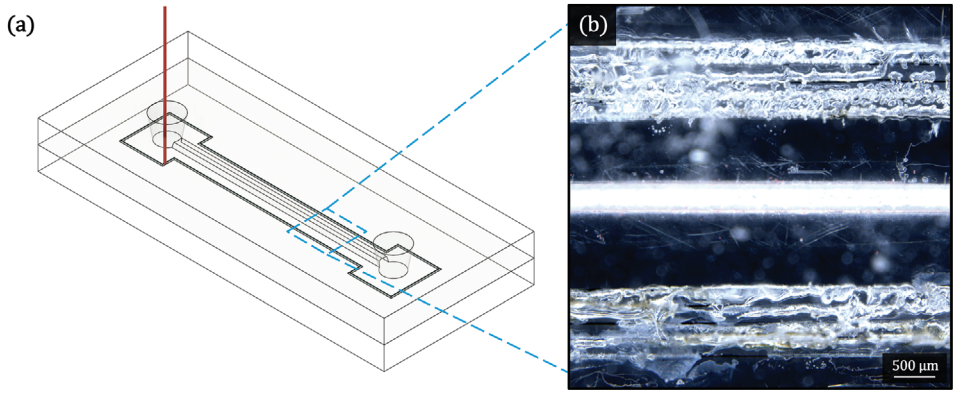

Figure 6. a) Schematic of the assembly of the hybrid PMMA-fused silica microfluidic chip. b) Optical microscope image in reflection mode of the sealed microfluidic channel at the interface.

in a pressure injection test. This outcome demonstrates that ultrafast laser transmission microwelding could provide superior pressure resistance and bonding reliability compared to other commonly used methods, highlighting its potential for high-pressure microfluidic applications.

3. Conclusion

This study successfully demonstrated the feasibility of joining polymethyl methacrylate (PMMA) and fused silica using femtosecond laser transmission welding. By systematically optimizing laser parameters, including peak fluence, scanning speed, and hatch distance, robust and reliable joints were achieved. A detailed analysis supported by SEM imaging and ATR-FTIR spectroscopy revealed that mechanical interlocking was the primary bonding mechanism. The formation of grooves on the fused silica surface, subsequently filled with melted and resolidified PMMA, created strong interfacial adhesion. The developed heat accumulation model confirmed that the distinct thermomechanical properties of the two materials resulted in non-thermal ablation for the fused silica and melting for the PMMA. This model also enabled accurate prediction of the laser-melted track widths in the PMMA under varying operating parameters, emerging as a promising tool for designing laser material processing experiments.

The practical viability of femtosecond laser transmission welding was further demonstrated through the successful application of this technique to seal a hybrid microfluidic chip, which withstood pressures up to 2 bar. The proposed laser-based method exhibited superior pressure resistance and bonding reliability compared to other common methods, highlighting its potential for fabricating robust microfluidic devices and other hybrid structures between polymers and transparent hard and brittle materials.

The possibility offered by the fs laser technology to be utilized in different machining steps, as drilling, milling, and welding, suggests the potential to develop a monolithic fabrication platform for LoC hybrid devices. This approach could enable straightforward and automatic processing of materials using a single light source coupled with a scanning head, eliminating the need for chemicals, masks, or intermediate steps.

4. Experimental Section

Samples and Clamping Configuration: In this study, high-purity optical-quality polymethyl methacrylate (PMMA) (Vistacryl CQ, Vista Optics Ltd) and fused silica (Nano Quarz Wafer GmbH) substrates were employed, each with an area of 24.5 × 24.5 mm^2 and a thickness of 1 mm. Both PMMA and fused silica were certified with $\lambda/4$ flatness and surface roughness of less than 5 nm. Prior to the bonding process, the PMMA samples underwent sonication in deionized (DI) water for 15 min. The substrates were stacked on top of each other and clamped together using a 4-point bolt system to ensure uniform pressure across their surfaces. Since the position of the clamps was observed to affect the diffusion of molten material, a consistent clamping configuration was maintained across all trials to reduce potential systematic errors.

Laser System: The light source employed was a femtosecond solid state laser system (PHAROS SP 1.5, Light Conversion) emitting a linearly polarized, almost diffraction-limited (M^2 = 1.3) laser beam at a nominal central wavelength of 1030 nm. In the present study, the pulse duration τ_P = 190 fs and repetition frequency f_r = 200 kHz were fixed, while the pulse energy E_P was finely tuned by a half-waveplate and a polarizer. The linearly polarized beam was focused on the interface between the two substrate surfaces with a *f*-theta lens of 100 mm focal length, coupled to a PC-controlled galvo scanner (IntelliSCANN 14, SCAN-LAB). The estimated beam waist ω in air was 16 µm.

Shear Break Test: The weld strength was evaluated using a custom shear break testing rig, schematized in Figure S1 (Supporting Information). The PMMA substrate was clamped to a fixed stage with half of the glass substrate extending over the edge of the stage, while a dynamometer (FK 250, Fr. Sauter AG) was mounted on a movable translational stage. In this push-test configuration, the dynamometer was manually pushed against the edge of the glass substrate until the joint broke. The bond shear strength *S* was calculated as the ratio between the force *F* registered at the breaking point and the weld area *A*: $S = F/A$. To ensure consistent and reproducible measurements, the welds always covered a fixed area $A = 5 \times 5$ mm^2, and the force was always applied parallel to the scanning lines.

Analyses of the Weld Seams: The morphology of the weld seams was assessed using an optical microscope (Nikon Eclipse ME600) and a scanning electron microscope (SEM, Sigma 560 VP, Zeiss). Infrared spectra of the weld seams and each pristine material were acquired using a Fourier Transform Infrared (FTIR) spectrometer (Nicolet iS50, ThermoFisher) in attenuated total reflectance (ATR). Spectra were collected from 500 to 4000 cm^{-1} by combining 32 sequential scans for noise reduction.

Fabrication and Testing of the Microfluidic Chip: The hybrid microfluidic chip featured a single straight microchannel, 1 cm in length, which connected two reservoirs with a diameter of 0.8 mm. The microchannel, measuring 300 µm in width and 200 µm in depth, was micromachined on the surface of the PMMA substrate using the same laser source and operating

parameters ($E_P = 8\,\mu J, f_r = 25\,kHz, v_s = 30\,mm\,s^{-1}, h = 3\,\mu m$) provided by Volpe et al.[41] The device was assembled by producing a weld seam that enclosed both the channel and the reservoirs, effectively sealing the entire device. For the static leakage test, the inlet was connected to a microfluidic flow controller (OB1 MK3+, Elveflow), operating between 0.01 mbar and 2 bar, and the outlet was clamped, as schematized in Figure S2 (Supporting Information). A solution of distilled water and red organic dye was injected into the microfluidic channel at increasing pressures in 100 mbar increments. Each pressure level was maintained for 120 s while a camera (AD7013MTL, 20-90X magnification, Dino-Lite) was used to monitor the channel in real-time for any signs of leakage.

Supporting Information

Supporting Information is available from the Wiley Online Library or from the author.

Acknowledgements

This work was supported by MUR in the framework of the PRIN 2022 PNRR Project "Surface and Interface acoustic wave-driven Microfluidic devices BAsed on fs-laser technology for particle sorting (SIMBA)" (grant number: Prot. P2022LMRKB) and the project "Quantum Sensing and Modeling for One-Health (QuaSiModO)" (CUP: H97G23000100001).

Open access publishing facilitated by Universita degli Studi di Bari Aldo Moro, as part of the Wiley - CRUI-CARE agreement.

Conflict of Interest

The authors declare no conflicts of interest.

Author Contributions

F.A.S. performed the conceptualization, investigation, formal analysis, visualization, and writing of the original draft. R.D.P. contributed to the investigation, formal analysis, visualization, and writing of the original draft. C.G. handled the writing – review and editing. P.P. contributed to the writing – review and editing, and supervision. A.A. was responsible for formal analysis and writing – review and editing. A.V. contributed to the conceptualization, formal analysis, visualization, writing – review and editing, and supervision. The authors would like to thank Domenico Cannatà and Pietro Paolo Calabrese for their technical support and Francesco Spadaro for his assistance during the investigation phase.

Data Availability Statement

The data that support the findings of this study are available from the corresponding author upon reasonable request.

Keywords

femtosecond lasers, fused silica, laser welding, microfluidics, polymethyl methacrylate, transmission welding

Received: September 27, 2024
Revised: October 31, 2024
Published online:

[1] U. Ali, K. J. B. A. Karim, N. A. Buang, *Polymer Reviews* **2015**, *55*, 678.
[2] Y. Chen, L. Zhang, G. Chen, *Electrophoresis* **2008**, *29*, 1801.
[3] S. T. Amancio-Filho, L. A. Blaga, *Joining of Polymer-Metal Hybrid Structures: Principles and Applications*, John Wiley & Sons, New Jersey **2018**, 127.
[4] F. Lambiase, S. I. Scipioni, C. J. Lee, D. C. Ko, F. Liu, *Materials* **2021**, *14*, 1890.
[5] J. Auerswald, P. Niedermann, H. Haquette, F. Dias, H. Keppner, H. F. Knapp, in *Encyclopedia of Microfluidics and Nanofluidics* (Ed: D. Li), Springer, Boston, MA, **2008**, https://doi.org/10.1007/978-0-387-48998-8_625.
[6] T. Matsumae, M. Nakano, Y. Matsumoto, T. Suga, *ECS Trans.* **2013**, *50*, 297.
[7] B. Acherjee, *J Manuf Process* **2021**, *64*, 421.
[8] Y. Huang, X. Gao, Y. Zhang, B. Ma, *J Manuf Process* **2022**, *79*, 934.
[9] S. Richter, F. Zimmermann, A. Tünnermann, S. Nolte, *Opt. Laser Technol.* **2016**, *83*, 59.
[10] S. Huang, R. Chen, H. Zhang, J. Ye, X. Yang, J. Sheng, *Opt. Laser Technol.* **2020**, *131*, 106427.
[11] J. Xu, Q. Jiang, J. Yang, J. Cui, Y. Zhao, M. Zheng, J. P. Oliveira, Z. Zeng, R. Pan, S. Chen, *Metals 2023* **2023**, *13*, 876.
[12] A. Volpe, F. Niso, C. Gaudiuso, A. Rosa, R. M. Vazquez, A. Ancona, P. Lugarà, R. Osellame, *Opt. Express* **2015**, *23*, 4117.
[13] G. L. Roth, S. Rung, R. Hellmann, *Opt Lasers Eng* **2017**, *93*, 178.
[14] F. M. C. Capodacqua, A. Volpe, C. Gaudiuso, A. Ancona, *Sci. Rep.* **2023**, *13*, 5062
[15] R. R. Thomson, J. D. Shephard, D. P. Hand, R. M. Carter, J. Chen, *Appl. Opt.* **2014**, *53*, 4233.
[16] P. Sopeña, A. Wang, A. Mouskeftaras, D. Grojo, *Laser Photon Rev* **2022**, *16*, 2200208.
[17] S. Baudach, J. Bonse, J. Krüger, W. Kautek, *Appl. Surf. Sci.* **2000**, *154–155*, 555.
[18] S. zhen Xu, C. zhen Yao, W. Liao, X. dong Yuan, T. Wang, X. tao Zu, *Nucl Instrum Methods Phys Res B* **2016**, *385*, 46.
[19] S. Richter, S. Döring, A. Tünnermann, S. Nolte, *Appl Phys A Mater Sci Process* **2011**, *103*, 257.
[20] H. Liu, H. Liu, W. Xu, H. Wang, X. Wang, *Ceram. Int.* **2022**, *48*, 11018.
[21] F. I. Hussein, E. Akman, B. Genc Oztoprak, M. Gunes, O. Gundogdu, E. Kacar, K. I. Hajim, A. Demir, *Opt. Laser Technol.* **2013**, *49*, 143.
[22] K. G. D. C. Monsores, A. O. Da Silva, S. De Sant'Ana Oliveira, J. G. P. Rodrigues, R. P. Weber, *J. Mater. Res. Technol.* **2019**, *8*, 3713.
[23] C. De Marco, S. Eaton, R. Suriano, S. Turri, M. Levi, R. Ramponi, G. Cerullo, R. Osellame, *ACS Appl. Mater. Interfaces* **2010**, *2*, 2377.
[24] R. Shanti, A. N. Hadi, Y. S. Salim, S. Y. Chee, S. Ramesh, K. Ramesh, *RSC Adv.* **2016**, *7*, 112.
[25] C. Le Losq, M. R. Cicconi, G. N. Greaves, D. R. Neuville, *Springer Handbooks*, Springer, Cham **2019**, 441.
[26] R. Weber, T. Graf, P. Berger, V. Onuseit, M. Wiedenmann, C. Freitag, A. Feuer, J. P. Negel, A. Voss, M. A. Ahmed, D. Bauer, D. Sutter, A. Killi, T. Graf, *Opt. Express* **2014**, *22*, 11312.
[27] B. Neuenschwander, B. Jäggi, M. Schmid, U. Hunziker, B. LüEscher, C. Nocera, *30th Int. Congress on Applications of Lasers and Electro-Optics, ICALEO*, AIP Publishing, **2011**, 783.
[28] A. Ben-Yakar, R. L. Byer, *J. Appl. Phys.* **2004**, *96*, 5316.
[29] W. D. Callister, D. G. Rethwisch, *Materials Science and Engineering: An Introduction*, Wiley, New Jersey **2018**.
[30] S. S. Mao, F. Quéré, S. Guizard, X. Mao, R. E. Russo, G. Petite, P. Martin, *Appl. Phys. A* **2004**, *79*, 1695.
[31] A. Ben-Yakar, R. L. Byer, A. Harkin, J. Ashmore, H. A. Stone, M. Shen, E. Mazur, *Appl. Phys. Lett.* **2003**, *83*, 3030.
[32] J. M. Liu, *Opt. Lett.* **1982**, *7*, 196.
[33] H. Jacobs, C. Momma, S. Nolte, A. Tünnermann, B. N. Chichkov, B. Wellegehausen, H. Welling, *JOSA B* **1997**, *14*, 2716.

[34] E. Mazur, *Advanced Photonics & Renewable Energy*, Optica Publishing Group, Washington, DC **2010**, p. BWB4.
[35] R. De Palo, A. Volpe, C. Gaudiuso, P. Patimisco, V. Spagnolo, A. Ancona, *Opt. Express* **2022**, *30*, 44908.
[36] F. A. Sfregola, R. De Palo, C. Gaudiuso, F. P. Mezzapesa, P. Patimisco, A. Ancona, A. Volpe, *Opt. Laser Technol.* **2024**, *177*, 111067.
[37] Y. Jee, M. F. Becker, R. M. Walser, *J. Opt. Soc. Am. B* **1988**, *5*, 648.
[38] Y. Yan, P. Zhou, H. Wang, Y. Mao, *Polymers* **2020**, *12*, 2122.
[39] M. Rasponi, F. Piraino, N. Sadr, M. Laganà, A. Redaelli, M. Moretti, *Microfluid Nanofluidics* **2011**, *10*, 1097.
[40] S. Bhattacharya, A. Datta, J. M. Berg, S. Gangopadhyay, *J. Microelectromech. Syst.* **2005**, *14*, 590.
[41] A. Volpe, P. Paiè, A. Ancona, R. Osellame, *Microfluid Nanofluidics* **2019**, *23*, 37.